

Article

Tunable Sensing and Transport Properties of Doped Hexagonal Boron Nitride Quantum Dots for Efficient Gas Sensors

Hazem Abdelsalam^{1,2}, Vasil A. Saroka^{3,4}, Mohamed M. Atta⁵, Omar H. Abd-Elkader^{6,*},
Nouf S. Zaghloul⁷ and Qinfang Zhang^{1,*}

¹ School of Materials Science and Engineering, Yancheng Institute of Technology, Yancheng 224051, China

² Theoretical Physics Department, National Research Centre, P.O. Box 21111, Giza 12622, Egypt

³ T Bpack Ltd., 27 Old Gloucester Street, London WC1N 3AX, UK

⁴ Institute for Nuclear Problems, Belarusian State University, Bobruiskaya 11, 220030 Minsk, Belarus

⁵ Radiation Physics Department, National Center for Radiation Researches and Technology (NCRRT), Atomic Energy Authority, Cairo 11787, Egypt

⁶ Department of Physics and Astronomy, College of Science, King Saud University, P.O. Box 2455, Riyadh 11451, Saudi Arabia

⁷ Bristol Centre for Functional Nanomaterial's, HH Wills Physics Laboratory, Tyndall Avenue, Bristol BS8 1FD, UK

* Correspondence: omabelkader7@ksu.edu.sa (O.H.A.-E.); qfangzhang@ycit.edu.cn (Q.Z.)

Abstract: The electronic, sensing, and transport properties of doped square hexagonal boron nitride (shBN) quantum dots were investigated using density functional theory calculations. The electronic and magnetic properties were controlled by substitutional doping. For instance, heterodoping with Si and C atoms decreased the energy gap to half its value and converted the insulator shBN quantum dot to a semiconductor. Doping with a single O atom transformed the dot to spin half metal with a tiny spin-up energy gap and a wide spin-down gap. Moreover, doping and vacancies formed low-energy interactive molecular orbitals which were important for boosting sensing properties. The unmodified shBN quantum dot showed moderate physical adsorption of NO₂, acetone, CH₄, and ethanol. This adsorption was elevated by doping due to interactions between electrons in the low-energy orbitals from the doped-shBN dot and π -bond electrons from the gas. The transport properties also showed a significant change in the current by doping. For instance, the spin-up current was very high compared to the spin-down current in the shBN dots doped with an O atom, confirming the formation of spin half metal. The spin-up/down currents were strongly affected by gas adsorption, which can be used as an indicator of the sensing process.

Keywords: hexagonal boron nitride quantum dots; doping; density functional theory; electronic; sensing; transport properties; gas sensor



Citation: Abdelsalam, H.; Saroka, V.A.; Atta, M.M.; Abd-Elkader, O.H.; Zaghloul, N.S.; Zhang, Q. Tunable Sensing and Transport Properties of Doped Hexagonal Boron Nitride Quantum Dots for Efficient Gas Sensors. *Crystals* **2022**, *12*, 1684. <https://doi.org/10.3390/cryst12111684>

Academic Editor: Xing-Wang Zhang

Received: 2 November 2022

Accepted: 18 November 2022

Published: 21 November 2022

Publisher's Note: MDPI stays neutral with regard to jurisdictional claims in published maps and institutional affiliations.



Copyright: © 2022 by the authors. Licensee MDPI, Basel, Switzerland. This article is an open access article distributed under the terms and conditions of the Creative Commons Attribution (CC BY) license (<https://creativecommons.org/licenses/by/4.0/>).

1. Introduction

A monolayer of hexagonal boron nitride (hBN) is a 2D material that is often referred to as 'white graphene'. A free-standing monolayer of hBN was successfully fabricated by a local electron beam thinning of a few-layer flake in 2009 [1,2], but it contained many lattice defects such as vacancies. Latter higher-quality single- and few-layer samples were produced by chemical vapor deposition on a Cu substrate [3,4]. A single layer of hBN has the same lattice structure as graphene and a commensurate lattice constant (1.45 Å vs. 1.42 Å in graphene). However, its band gap is significantly larger owing to polar covalent B-N bonds and exceeds 5 eV [3,5]. It has a high elastic constant (200–500 N/m) [3] and high thermal conductivity (227–280 W·m⁻¹·K⁻¹) [6]. Similar to graphene, a free-standing hBN membrane is thermally stable and chemically inert unless the temperature is increased above 1000 °C [7] or defects and metallic surfaces are introduced to increase its catalytic activity [8]. Monolayer hBN is a perfect material for a variety of applications. In addition to the applications naturally

inherited from bulk hBN, such as ultraviolet emitter [9,10], transparent membrane, dielectric, and protective coating applications [11,12] owing to its ultraflat and charge-impurity-free surface, monolayer hBN is a perfect atomically smooth substrate that allows preserving the intrinsic electrical and optical properties of other 2D materials [13]. This also makes it an important component of Van der Waals heterostructures in 2D materials [14]. The low-loss dielectric properties in the microwave and optical regimes make monolayer hBN a promising material for superconducting circuits and qubits [15], single-photon quantum emitters [16–19], and low-loss polaritonics [20], especially when isotopically purified [21]. Modifying the structure of an hBN sheet or producing hybrid BNC structures opens the possibility to tailor the pure hBN sheet electronic properties and reduce the band gap [22–27]. Similar to graphene, monolayer hBN can form lower dimensional structures such as 1D tubes, ribbons, or 0D quantum dots (QDs) [5]. The structures with edges are of particular interest since they may possess peculiar magnetic and electrical properties that are useful in spintronics and sensing devices [28,29]. While high-quality samples of both hBN tubes and ribbons have been around for more than a decade (tubes were synthesized in 1995 [30,31], and ribbons were synthesized in 2010 [23]), the similar-quality samples of small flakes have become available only quite recently. The past few years have seen dramatic developments in a variety of techniques for the synthesis of few-layer [32–39] and monolayer [40–42] hBN QDs. The first experimental studies of hBN QDs demonstrated their good biocompatibility, low cytotoxicity, and great potential for metal ion detection [43]. This naturally ignited curiosity about hBN QDs' intrinsic properties and potential applications. Similar to graphene or silicene QDs [44,45], the properties of hBN QDs depend on the shape, size, and edge morphology [46]. However, an additional binary degree of freedom arises owing to their heteroatom nature. hBN QD edges can be terminated with B or N atoms, and this can drastically affect their stability, edge chemistry [47–49], and electronic properties [50–56]. A range of topics were covered in theoretical studies, even before the synthesis of hBN QDs; for instance, it has been shown that hBN nanoribbon-based QDs possess higher thermopower and lower phonon thermal conductance than graphene quantum dots with the same geometry parameters [57]. This has allowed researchers to deploy them for improving heat dissipation in white QDs-LEDs, avoiding the degradation of optical properties [58,59]. Moreover, there have been substantial theoretical data gathered on hBN QD's physical and chemical adsorption and sensing properties. For instance, the electronic and optical properties of hBN QDs are sensitive to the physisorption of tetracyanoquinodimethane and tetrathiafulvalene [60]. Such dots also exhibit good adsorption properties for several gases (H_2 , CO, NO, O_3 , H_2O , and O_2), especially when functionalized with metal-oxide complexes (CuO, AgO, and AuO) [61]. This, in particular, shows their great potential for reversible H_2 storage. It has also been shown that functionalization with more complex metal clusters (OLi₄, NLi₅, CLi₆, BLi₇, and Al₁₂Be) is energetically favorable, and it significantly affects the optical transition energies, so substantial nonlinear optical activity can be expected from hBN QDs [55]. A strain-tunable ammonia nanosensor was theoretically proposed as early as 2013 [62]. Recently, the ammonia sensitivity has been corroborated by chemical sensing studies [63]. As we have shown in our previous work, hBN QDs are capable of adsorbing or bonding with a range of hydrated transition and heavy metals (Cd, Co, Cr, Cu, Fe, and Zn) [64]. Such adsorption processes can be further enhanced by chemical functionalization, for instance, with COOH groups that give additional stability to the hBN QD structure. Hence, similar to boron nitride foam-like porous monoliths [65], hBN QDs carry great potential for water purification. The first experimental indication of this was recently obtained [66].

Substitutional doping is an efficient route to modify the properties of QDs [67,68]. However, while some research on hBN QDs' substitutional doping with C atoms is available [52–54,69], the contemporary literature lacks information on the effects of other elemental doping. At the same time, it has recently been shown that the substitution doping of an hBN monolayer with sulfur increases its conductivity up to 1.5 times and enhances the optoelectronic properties compared to pristine hBN [70]. This has allowed the authors of Ref. [70] to fabricate a photodetector with a broadband response (260–280 nm wavelength)

and a 50 times increased photocurrent. It was identified that the main improvement comes from enhanced light absorption and reduced resistivity mainly due to N atoms being replaced with sulfur. Motivated by these recent achievements and the current white spots in the literature on hBN QDs, we have performed a systematic study of single atom (O, P, and Si) and heteroatom (P-C and Si-C) doping of square hBN (shBN) QDs and their transport properties. This investigation is also supplemented by an important case study of the vacancy defect that seems to play a key role in recently reported quantum light sources and may be useful for solid-state qubits and quantum sensors [71,72]. Our results show that the electronic, sensing, and transport properties of shBN QDs can be smoothly controlled and improved by doping, making them potential active elements of gas sensors.

2. Computational Model

The current density functional theory calculations were performed using Gaussian 16 software [73] using the B3LYP functional [74,75] and the 6–31 g basis set [76,77]. This moderate level of theory was tested and was found to be good with respect to higher levels of theory when considering both computational power and result accuracy [64]. The Van der Waals interactions between the shBN QDs and the adsorbed gases were accounted for through the inclusion of Grimmes’s dispersion correction (gd3) to the B3LYP functional [78]. The considered model was a square nanoflake from hBN with a total number of atoms equal to 74 and a net spin equal to zero. Thus, closed-shell calculations were used. After doping or vacancy creation, the net spin may increase. In this case, we performed spin-polarized open-shell calculations.

3. Results and Discussion

3.1. Electronic Properties

The effects of substitutional doping and defects on the electronic, sensing, and transport properties of shBN QDs were considered. The shBN QD was chemically modified by three means: (a) by doping with a single atom of O, P, or Si, as seen in Figure 1a–c; (b) by vacancy formation (Figure 1d); or (c) by doping with two atoms such as P and C or Si and C, as shown in Figure 1e,f. In what follows, we investigated the effects of doping and defects on the electronic properties by considering the partial density of states of the selected structures. In addition, the distributions of the highest occupied/lowest unoccupied molecular orbitals (HOMOs/LUMOs) were considered.

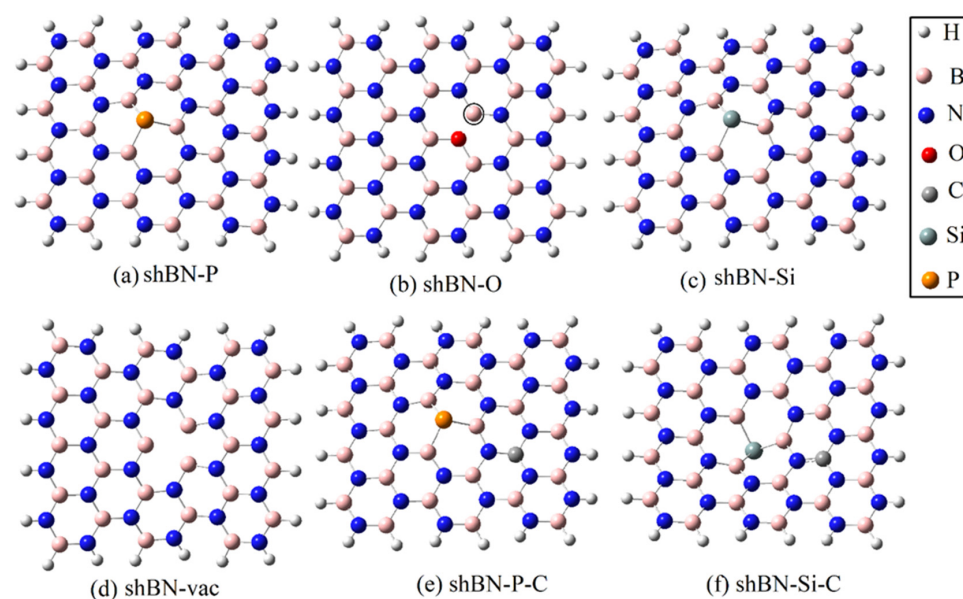


Figure 1. Optimized structures of shBN QDs with single-atom doping (a–c), one-atom vacancy (d), and two-atom doping (e,f). Circle: B atom hosting an unpaired electron.

The partial density of states (PDOS) of doped and defected shBN QDs are shown in Figure 2. It is observed from Figure 2a that doping with P atoms did not change the energy gap or the density of states significantly from those of the unmodified shBN QDs. Our recent work [79] showed that shBN QDs of similar size had an energy gap of ~ 5.82 eV, which was comparable to the 5.70 eV in shBN-P QD in Figure 2a. The density of states was also similar due to the small contribution of the doped P atom. A considerable effect of doping started to appear when doping with O and Si atoms. The doping atoms lifted the degeneracy between the spin-up (α) and spin-down (β) molecular orbitals, leading to a very small spin-up energy gap of 0.77 eV (Figure 2b) in shBN-O QDs or a moderate energy gap of 2.62 eV in shBN-Si QDs (Figure 2c). Thus, the insulating shBN QDs could be converted to half metallic in shBN-O QDs, which were conductors for spin-up electrons and insulators for spin-down electrons.

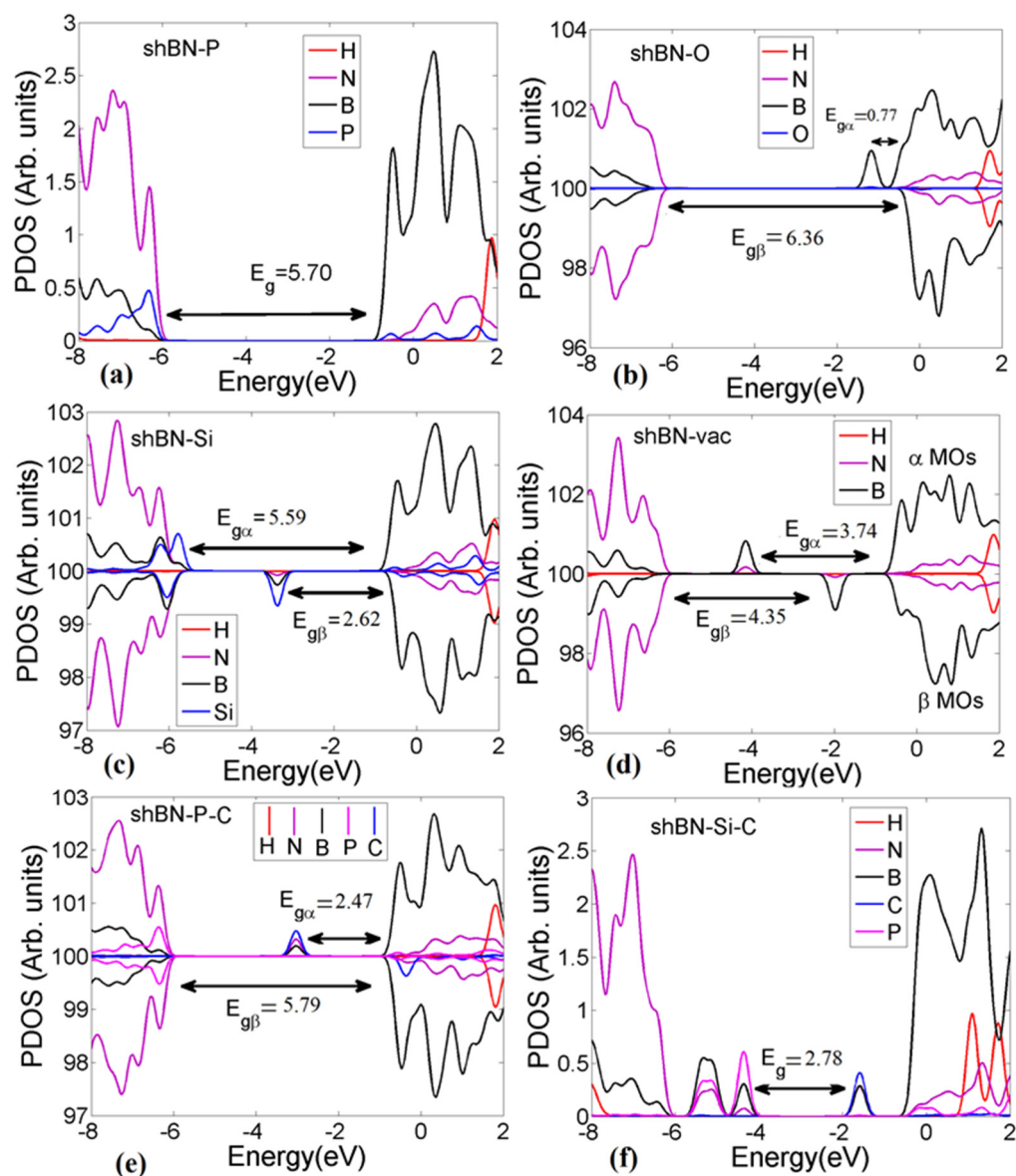


Figure 2. The partial density of states doped and defected shBN. (a–c) Doping with single atoms, (d) shBN with a single vacancy, and (e,f) doping with two atoms.

The two unpaired electrons from the doping O atoms formed two covalent bonds with those from neighboring B atoms, leaving an unpaired electron on one of the three neighboring B atoms, as shown in Figure 1b. This free radical electron formed a half-filled spin-up orbital that is represented by the black peak decreasing the energy gap in Figure 2b.

The case of shBN-Si QD was different, where the half-filled molecular orbital came from the fourth unpaired electron in the sp^3 -hybridized Si atom. The partial density of states for a single vacancy and doping with two atoms presented in Figure 2d–f also shows that the energy gap decreased as a result of the evolution of low-energy states from atoms around the vacancy or the doping atoms. Similar to the effect of doping on the energy discussed above, vacancy creation also decreased the energy gap. Removing one N atom at the surface led to the breaking of three B–N bonds, which in turn led to the formation of unpaired interactive electrons in the neighboring B atoms. The interactive electrons formed low-energy molecular orbitals, represented by the low-energy black peak in Figure 2d, that eventually decreased the energy gap.

The HOMO/LUMO distributions in Figure 3 show a schematic presentation of the effect of doping on the low-energy molecular orbitals. Starting from the unmodified shBN QD in Figure 3a, the HOMOs were localized and distributed on N atoms, which means that it originated from the lone pairs of N atoms [79]. The LUMOs were distributed on B atoms, meaning that an electronic transition would be to the unoccupied molecular orbitals of B atoms. Similar to the PDOS distribution, doping with P atoms had a negligible effect on the distribution of the HOMOs compared to its distribution on undoped shBN QDs. The only difference was that the LUMOs were distributed not only on B atoms but also on the doping P atom. Doping with O atoms significantly changed the distribution of the spin-up HOMOs, as shown in Figure 3c. It was distributed on the B atoms, confirming its origin from the unpaired electron on B atoms. The spin-up LUMO and the spin-down HOMO/LUMO distributions were similar to those of undoped shBN QDs, which confirmed the results obtained from the PDOS. The special case of shBN-Si QDs in Figure 3d shows that the spin-up and spin-down HOMOs were mostly distributed on the Si atom and neighboring atoms. This means that not only did the unpaired electrons from the Si atom form the spin-down HOMOs that decreased the spin-down energy gap but the Si–B bond was weaker than the in-plane B–N bond and formed the spin-up HOMOs. The unpaired electrons on B atoms formed by removing one N atom were responsible for the spin-up HOMO distribution around the vacancy in the shBN-vac QD in Figure 3e. The other low-energy molecular orbitals were similar to that of unmodified shBN QDs, except for the spin-down LUMOs that were formed by B atoms around the vacancy and were distributed on them. The shBN-P-C QD in Figure 3 shows that adding a C atom to an shBN-P QD (Figure 3b) significantly changed the spin-up distribution on and around the C atom due to its unpaired pi-electron.

3.2. Sensing Properties

The energy gap decreasing and the low-energy molecular orbitals with interactive electrons formed by doping or vacancy were expected to significantly enhance the sensing and catalytic properties of shBN QDs. Here, we studied the adsorption properties of different gases, including NO_2 , CH_4 , acetone, and ethanol, to clarify the effects of doping and vacancy on the sensing properties. Figure 4 shows the optimized structures of shBN QDs adsorbing different gases before and after chemical modification. For the adsorption, we choose two initial positions around the N atom. That atom was replaced in the case of doping or removed in the case of vacancy formation (Figure 4a). These positions gave the best representation of the effect of modification on the adsorption properties. For large gas molecules such as acetone and ethanol, we chose only the intermediate position. The adsorbed gases were categorized into two groups: (a) gases with sp^2 hybridization, including NO_2 and acetone (acet.), and (b) gases with sp^3 hybridization, such as CH_4 and ethanol (eth). Some examples of the adsorption of the first group by the modified shBN QDs are shown in Figure 4b–i, while examples of the adsorption of the second group are shown in Figure 4j–m.

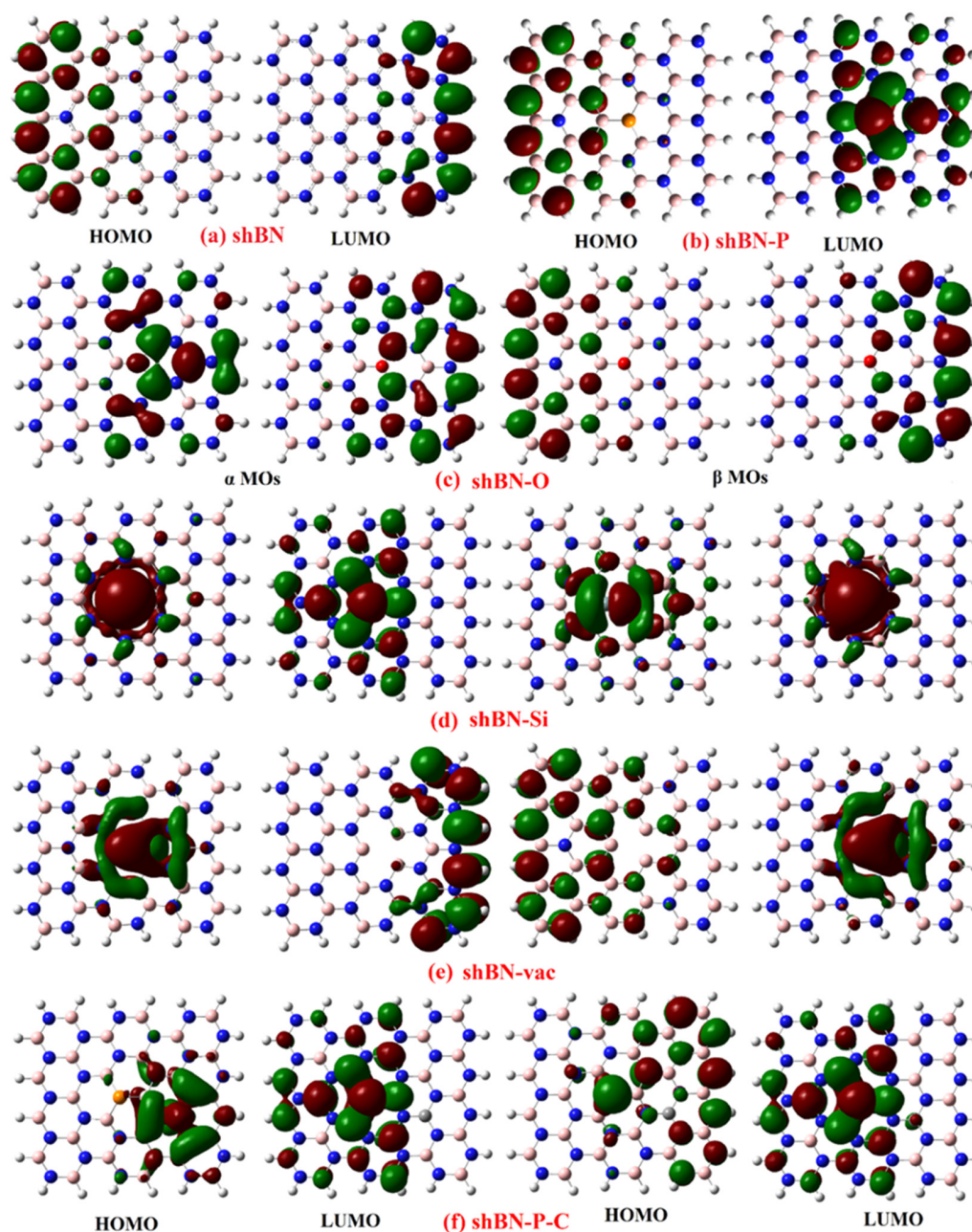


Figure 3. The HOMO and LUMO distributions of shBN QDs before (a) and after doping and vacancy formation.

Starting with the adsorption of the first group, it was observed that NO_2 and acetone were physically adsorbed on the surface of the shBN QDs (Figure 4b,c). The adsorption distances (d) in these cases were equal to ~ 2.9 and 3.1 Å, respectively. Doping with O atoms, see Figure 4d–f, converted the weak physical adsorption to strong chemical adsorption, with strong chemical bonds between the gas and the unpaired electron from the B atom around the dopant. In this case, the adsorption distance decreased to 1.5 Å. We chose two different adsorptions, as shown in Figure 4a, to account for different possibilities of interactions between the gas and the surface of the shBN QD. For instance, the adsorption of NO_2 can be through bonding with one O atom, as shown in Figure 4d for an shBN- NO_2 -a QD, or through bonding with N and O atoms, as in adsorption site b shown in Figure 4b. All the dopants considered in this work increased the interactions between the shBN surface and the gases. Only doping with P atoms showed a slight increase in the adsorption due to the slight change in the density of states. The adsorption energy per

atom (E_a), the charge transfer (Q), and the adsorption distance (d) given in Table 1 are good descriptors of adsorption strength. The E_a was calculated from $E_a = (E_{\text{gas}} + E_{\text{shBN}}) - E_{\text{gas + shBN}}$, where E_{gas} and E_{shBN} are the ground state energy of the gas and the shBN QD, respectively. $E_{\text{gas + shBN}}$ are the ground state energies of the gas and the shBN QD after adsorption. Accordingly, a negative value of E_a implies successful gas adsorption, and a higher absolute value of E_a means higher adsorption strength. The adsorption energy of NO_2 started at 0.32 eV in the unmodified shBN QDs and increased by doping, reaching its highest value of $E_a \sim 4.95$ eV in the case of doping with O atoms.

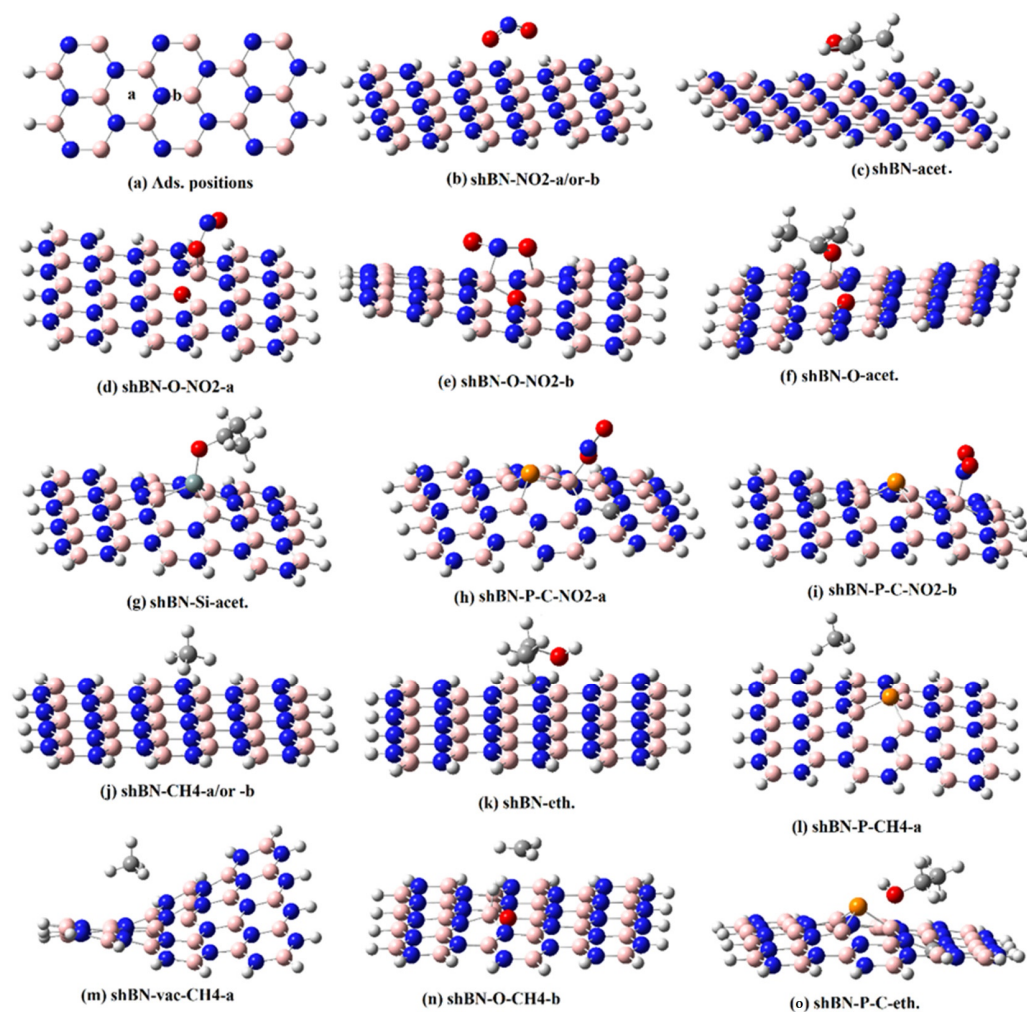


Figure 4. (a) The adsorption positions on which gases were adsorbed on the surfaces of shBN QDs. (b–o) The optimized structures of the shBN QDs adsorbing different gases, namely NO_2 , acetone (acet), CH_4 , and ethanol (eth), before and after chemical modification.

The adsorption of acetone was also improved by doping, reaching its highest values in the shBN-O QDs and the shBN-vac QDs, with adsorption energy values equal to 2.94 eV and 2.30 eV, respectively. The corresponding adsorption distance decreased from 2.9 Å in the shBN-acet QD to 1.46/1.39 in shBN-O-acet/shBN-vac-acet QDs due to the formation of strong bonds between the O atom from acetone and the B atoms around the dopant or the vacancy. Q in Table 1 is the total Mulliken charge on the gas, representing the amount of charge transferred to the gas (if negative) or from it (if positive) to the shBN QD. As given in Table 1, a moderate charge transferred from the unmodified shBN QDs to NO_2 with $Q \sim -0.40$ (e), and a small charge transferred to acetone ($Q = -0.02$ (e)). Doping and vacancy creation significantly enhanced the charge transfer. For instance, the small charge transfer from the shBN QD to acetone increased to -0.19 (e) in the shBN-Si-acet QD. Moreover,

charge transfer to NO₂ could be duplicated by doping with O atoms or double doping with P and C atoms, as given in Table 1.

Table 1. NO₂ and acetone adsorption on shBN. The adsorption energy (E_a), the gas distance above the surface of the shBN QD, the charge transferred to or from the gas (Q), the energy gap (E_g), and the total electric dipole moment (TEDM).

| Struct. | E _a (eV) | d (Å) | Q (e) | E _g (eV) |
|------------------------------|---------------------|-------|-------|---------------------|
| shBN (reference) | – | – | – | |
| shBN-NO ₂ -a | 0.32 | 2.88 | −0.34 | 3.07 α, 1.95 β |
| shBN-NO ₂ -b | 0.32 | 3.07 | −0.39 | 2.98 α, 1.85 β |
| shBN-acet | 0.68 | 2.91 | −0.02 | 5.61 |
| shBN-P-NO ₂ -a | 0.38 | 2.91 | −0.25 | 3.35 α, 2.16 β |
| shBN-P-NO ₂ -b | 0.28 | 2.93 | −0.17 | 3.55 α, 2.37 β |
| shBN-P-acet | 0.61 | 2.93 | 0.002 | 5.49 |
| shBN-vac-NO ₂ -a | 2.07 | 1.57 | −0.54 | 4.29 |
| shBN-vac-NO ₂ -b | 4.07 | 1.43 | −0.40 | 3.17 |
| shBN-vac-acet. | 2.30 | 1.39 | −0.14 | 3.51 |
| shBN-O-NO ₂ -a | 4.95 | 1.57 | −0.53 | 4.62 |
| shBN-O-NO ₂ -b | 1.53 | 1.53 | −0.61 | 4.22 |
| shBN-O-acet | 2.94 | 1.46 | −0.38 | 3.75 α, 5.67 β |
| shBN-Si-NO ₂ -a | 2.42 | 1.90 | −0.52 | 4.34 |
| shBN-Si-NO ₂ -b | 2.72 | 1.80 | −0.53 | 3.77 |
| shBN-Si-acet | 0.64 | 1.81 | −0.19 | 2.45 α, 3.93 β |
| shBN-P-C-NO ₂ -a | 2.99 | 1.55 | −0.73 | 4.19 |
| shBN-P-C-NO ₂ -b | 2.17 | 1.67 | −0.66 | 2.97 |
| shBN-P-C-acet | 0.67 | 2.71 | 0.02 | 2.44 α, 5.58 β |
| shBN-Si-C-NO ₂ -a | 1.59 | 1.54 | −0.51 | 3.41 α, 3.16 β |
| shBN-Si-C-NO ₂ -b | 0.99 | 1.98 | −0.55 | 1.41 α, 4.18 β |
| shBN-Si-C-acet | 0.84 | 2.83 | 0.003 | 3.08 |

The values of Q in Table 1 indicate that charge transfer occurred from the shBN nanoflakes to the adsorbed gases in all cases except for acetone. The direction of charge transfer from or to shBN nanoflakes to or from the gases can be understood from the position of the HOMO and LUMO of the gases in the spectrum of the electronic density of states. If the HOMO of the adsorbate was higher than the Fermi level of the pure adsorbent (shBN QD), there was a charge transfer to the adsorbent. If the LUMO was below the Fermi level, charges were transferred to the adsorbate [80].

The Fermi level (E_f) of the shBN QD was calculated from $E_f = (E_{\text{HOMO}} + E_{\text{LUMO}})/2$, where E_{HOMO} and E_{LUMO} are the HOMO and LUMO energies, respectively. For instance, the Fermi level of the shBN-P QD was ~ −3.44 eV, as seen in Figure 2a. The energy of the LUMO of NO₂ equals −4.40 eV, which was lower than the Fermi level of the shBN-P QD. Hence, charges transferred from the shBN-P QD to NO₂. Since the Fermi energy of the shBN-P QD was the lowest for all considered structures, charges were transferred from the considered structures to NO₂. Charge transfer was also determined by the degree of mixing between the HOMO and LUMO of the gases and the shBN QD orbitals. This could be the reason for the opposite charge transfer in some cases, such as the charge transfer from acetone to the shBN-P-C QD. The position of the adsorbate HOMO and LUMO and their mixing with the shBN QD orbitals can be determined from the PDOS plots and the HOMO distributions shown in Figure 5 for selected structures. Starting with the adsorption on the unmodified shBN QD, the contribution of NO₂ to the occupied molecular orbitals in the shBN-NO₂ QD was found to be deep in the conduction band and started at an energy of ~ −8 eV, as seen in Figure 5a. This was confirmed by the distribution of HOMOs only on the shBN QD in Figure 5g. On the other hand, the unoccupied orbitals of NO₂ appeared as the LUMOs for both the spin-up and spin-down states, such as the spin-up LUMO shown in Figure 5g. The same case is observed in Figure 5b for the shBN-acet QD with the occupied molecular orbitals of acetone below the HOMO, and its unoccupied orbitals

start as the LUMO of the shBN-acet QD. The strong chemical adsorption of NO₂ in the shBN-O-NO₂ complex showed different behavior, where the HOMO was contributed by the shBN-O QD and NO₂, as shown in Figure 5c,i. Due to the strong chemical adsorption, the contribution from acetone orbitals dominated the HOMO of the shBN-O-acet QD as seen in Figure 5d,j,l. In all the discussed cases, the occupied/unoccupied orbitals of the gas were below the HOMO/LUMO of the net system or contributed to it. The only case in Figure 5 where the unoccupied orbitals of the gas was higher than the LUMO of the net system was the shBN-P-C-acet QD in Figure 5f. This alignment was the reason for the opposite charge transfer from acetone to the shBN nanoflake. Regarding the adsorption of the second group, the unmodified shBN QD also showed moderate adsorption of CH₄ and ethanol, which were physically adsorbed at a relatively high adsorption distance, as seen in Table 2. Doping slightly affected the adsorption energy and charge transfer of this group because of the strong sigma bonds between the gas atoms that preferred to interact physically with the shBN QD, even after doping. Due to the moderate interaction, the energy gap experienced almost no change in some cases, such as shBN-CH₄ and shBN-P-CH₄ QDs. In the other adsorption cases that involved symmetry breaking between spin-up and spin-down electrons due to unpaired electrons from the gas or the dopant, the spin-up/-down energy gaps significantly changed, as given in Table 2.

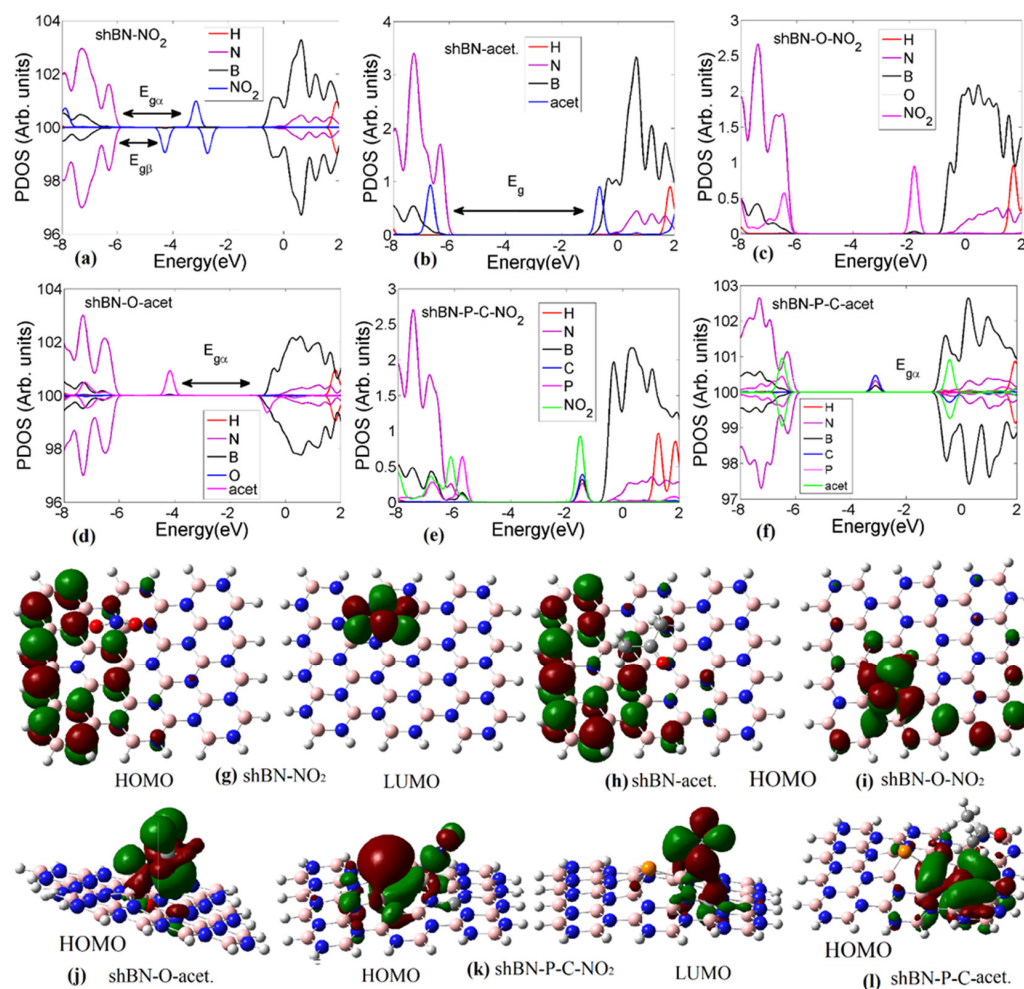


Figure 5. (a,b) Partial density of states of shBN QDs after adsorption of NO₂ and acetone. (c–f) The same in (a,b) but after doping shBN QDs with O or P–C atoms. The corresponding HOMO and selected LUMO distributions are shown in (g–l), and the distributions are shown for spin-up orbitals for the cases with the magnetic ordering of spins.

Table 2. CH₄ and ethanol adsorption on the shBN QD. The adsorption energy (E_a), the charge transferred to the gas (Q), the distance between the gas and the surface of the shBN QD (d), the energy gap (E_g), and the total electric dipole moment (TEDM).

| Struct. | E _a (eV) | Q (e) | d (Å) | E _g (eV) |
|------------------------------|---------------------|--------|-------|---------------------|
| shBN-CH ₄ -a | 0.19 | −0.007 | 2.90 | 5.82 |
| shBN-CH ₄ -b | 0.20 | −0.005 | 3.01 | 5.82 |
| shBN-eth | 0.57 | 0.012 | 2.69 | 5.87 |
| shBN-P-CH ₄ -a | 0.19 | −0.008 | 3.01 | 5.74 |
| shBN-P-CH ₄ -b | 0.19 | −0.007 | 2.99 | 5.75 |
| shBN-P-eth | 0.63 | 0.018 | 2.78 | 5.68 |
| shBN-vac-CH ₄ -a | 0.28 | −0.008 | 3.03 | 3.72 α, 4.17 β |
| shBN-vac-CH ₄ -b | 0.19 | −0.009 | 2.97 | 3.78 α, 4.27 β |
| shBN-vac-eth | 0.71 | 0.015 | 3.01 | 3.80 α, 4.16 β |
| shBN-O-CH ₄ -a | 0.59 | −0.037 | 2.76 | 2.20 α, 5.93 β |
| shBN-O-CH ₄ -b | 0.34 | 0.008 | 3.11 | 5.59 α, 4.54 β |
| shBN-O-eth | 1.09 | 0.012 | 2.49 | 2.21 α, 6.04 β |
| shBN-Si-CH ₄ -a | 0.19 | −0.006 | 2.89 | 5.27 α, 2.59 β |
| shBN-Si-CH ₄ -b | 0.18 | −0.003 | 3.00 | 5.28 α, 2.59 β |
| shBN-Si-eth | 0.59 | −0.019 | 2.14 | 5.20 α, 2.66 β |
| shBN-P-C-CH ₄ -a | 0.22 | −0.012 | 2.79 | 2.47 α, 5.78 β |
| shBN-P-C-CH ₄ -b | 0.19 | −0.006 | 3.04 | 2.46 α, 5.78 β |
| shBN-P-C-eth | 0.69 | 0.030 | 2.51 | 2.51 α, 5.78 β |
| shBN-Si-C-CH ₄ -a | 0.22 | −0.007 | 2.96 | 2.85 |
| shBN-Si-C-CH ₄ -b | 0.19 | −0.01 | 3.01 | 2.82 |
| shBN-Si-C-eth | 0.61 | 0.005 | 2.87 | 2.89 |

3.3. I-V Characteristics

Studying transport properties is very important to show the possible changes in the conductance due to gas adsorption, which can be used as an indicator of the adsorption process. Moreover, enhancing the efficiency of a gas sensor is related to boosting its conductivity, which can also be known from the transport properties. Here, we consider molecular conduction using the model proposed by P. Szarek et al. in which the charge transport through a molecule results from electrostatic induction [81]. In this case, the tunneling current (I) passing through the molecule can be calculated based on the uncertainty principle using the following equation:

$$I \leq \frac{2e\Delta N\Delta E}{\hbar} \quad (1)$$

where e is the electronic charge, \hbar is Planck's constant, ΔN is the valance electrons involved in the conduction, and ΔE is the energy change. ΔN is given by:

$$\Delta N = \frac{1}{2} \frac{\mu_E - \mu_0}{\eta_E + \eta_0} \quad (2)$$

The difference $\mu_e - \mu_0$ represents the difference in the electrochemical potential on the molecule due to the applied potential. η is the chemical hardness, and the term $\frac{1}{2} \left(\frac{1}{\eta_E + \eta_0} \right)$ represents the equivalent capacitance built-up in a molecule subjected to an external field. Both the chemical potential and hardness can be calculated from the energies of the HOMO and LUMO [82]. ΔE is the variation in the electrostatic energy due to the variation in the dipole moment ($\Delta \vec{D}_e$) in the direction of the applied electric field (\vec{E}_e), namely $\Delta E = -\Delta \vec{D}_e \cdot \vec{E}_e$. The change in the voltage (ΔV) was obtained directly from the applied field using $\Delta V = -E_e d$, where d is the length of the shBN QD in the direction of the applied electric field. We used this simple definition, which fixes the value of V in the I-V curves for all structures to make it easy to compare the current before and after doping and gas adsorption.

The current–voltage (I–V) characteristics were investigated before and after doping, as shown in Figure 6a, to show the effect of doping on the conductance. The changes in the current due to the adsorption of different gases, which can be used as an indicator of the occurrence of the absorption process, are shown in Figure 6b–d. Starting with Figure 6a, it was observed that there was a significant change in the current after doping. For instance, the spin-up current of the shBN–O QD was significantly higher than the current of the pure shBN QD, as shown in the insets of Figure 6a. Thus, doping the shBN QD with an odd number of O atoms converted it to a spin half metal, where the material was a conductor for electrons with spin up and a semiconductor for electrons with spin down. The noticeable change in the spin-up/spin-down current after doping with an O atom resulted from the considerable change in the energy gap, as discussed before. Similarly, single-atom doping with a Si atom and heteroatom doping with Si and C atoms increased the current due to the decrease in the electronic energy gap.

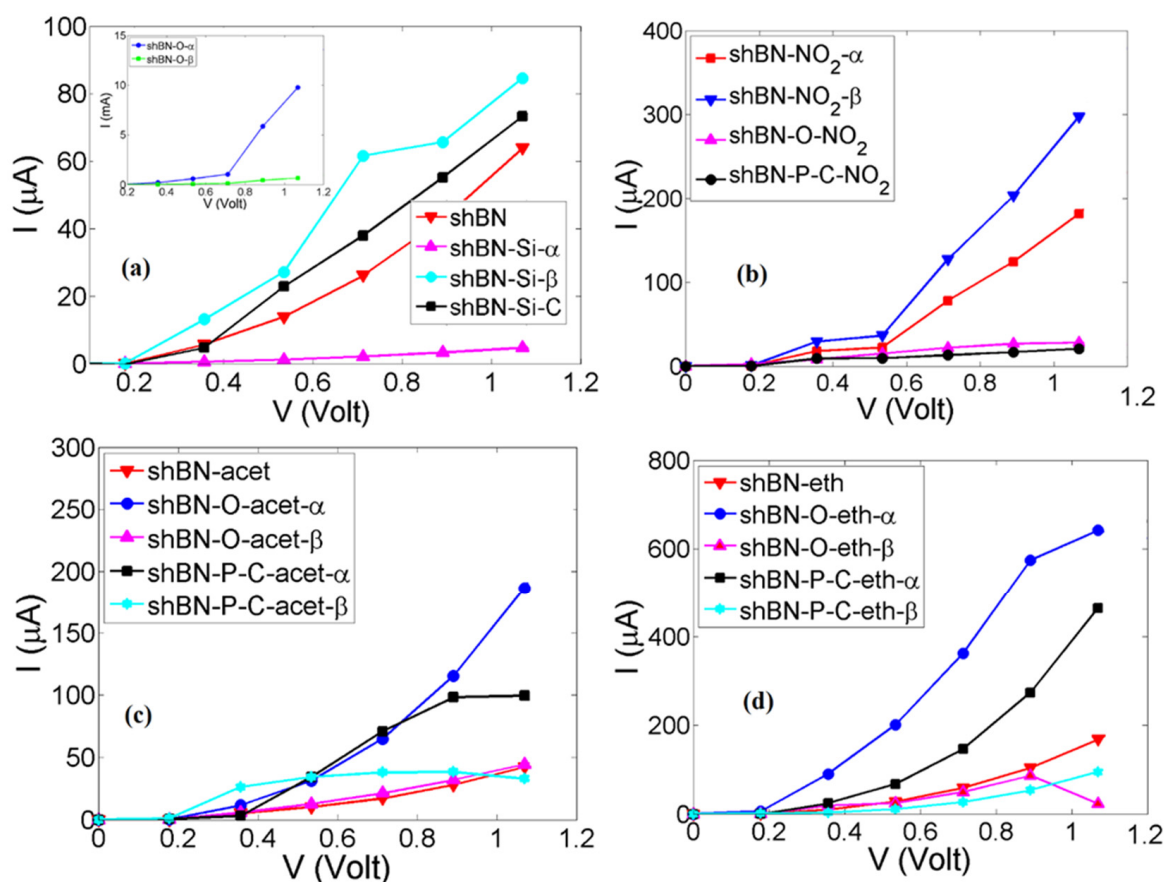


Figure 6. I–V curves of (a) the shBN QD before and after doping and (b–d) the shBN QD (with and without doping) after the adsorption of NO₂, acetone, and ethanol, respectively.

The effect of gas adsorption on the I–V curves shows that the high spin-up current of the shBN–O QD significantly decreased with the adsorption of NO₂ (Figure 6b). This was because of the passivation of the unpaired electron in the shBN–O QD by the unpaired electron from NO₂, which eventually restores the nonmagnetic ordering of the spin and increased the energy gap to $E_g = 4.62$ eV, as given in Table 1. In contrast, the current of the shBN QD was significantly enhanced after the adsorption of NO₂ due to the transformation to the ferromagnetic ordering of the spin with spin-up/-down energy gaps lower than that of the shBN QD. Since the shBN–P–C–NO₂ QD had an energy gap similar to that of the shBN–O–NO QD, their currents in Figure 6b were almost the same. The current representing the adsorption of acetone and ethanol was significantly affected by doping, as seen in Figure 6c,d. For instance, the spin-up current of the shBN–O–eth QD was considerably

higher than that of the shBN-eth QD, while the spin-down current was slightly lower than that of the shBN-eth QD. This was mainly due to the changes in the spin-up/-down energy gaps, as shown in Table 2. Thus, the I-V curves show that gas adsorption can be tracked by the significant change in the current. In addition, the enhanced conductivity implies that the considered systems are promising candidates for building efficient gas sensors [83].

4. Conclusions

In this work, we investigated the electronic, sensing, and transport properties of square hBN quantum dots (shBN QDs) doped with single atoms (O, P, and Si) and heteroatoms (P-C and Si-C). The effect of a single vacancy was also considered. The electronic properties were strongly affected by doping, where the energy gap decreased from ~5.7 eV in the unmodified shBN QD to 2.8 eV after doping with Si-C atoms. Additionally, the insulator shBN QDs could be converted to half metal by substitutional doping with a single O atom with a spin-up energy gap of 0.77 eV and a spin-down gap of 6.36 eV. Dopants or vacancies increased the number of low-energy peaks around the Fermi level, which not only decreased the energy gap but also enhanced the adsorption capability of shBN QDs. The sensing properties of the shBN QDs toward NO₂, acetone, CH₄, and ethanol gases were studied. The unmodified shBN QD showed moderate adsorption energy and charge transfer due to the physical adsorption on its surface. Substitutional doping and vacancy defects slightly enhanced the adsorption of CH₄ and ethanol due to the strong sp³ bonding in these gases, which made the gases interact physically with the adsorbent. On the other hand, the adsorption of NO₂ and acetone strongly improved by doping due to the interactions between the low-energy molecular orbitals from the doped shBN QD and the interactive pi-bond electrons from NO₂ and acetone. The I-V characteristics showed that the current moderately increased by doping with Si-C or greatly increased (spin-up current) by doping with an O atom. This means that the conductivity of the shBN QDs can be boosted by doping, which is crucial for efficient sensor applications. After adsorption, the current showed a noticeable increase/decrease, which can be used as an indicator for the adsorption process. Thus, substitutional doping or vacancy defects are reliable tools to tune the electronic and sensing properties of shBN QDs to build efficient gas sensors.

Author Contributions: Conceptualization, H.A. and Q.Z.; methodology, V.A.S.; software, M.M.A.; validation, H.A., M.M.A. and V.A.S.; formal analysis, O.H.A.-E.; investigation, H.A.; resources, O.H.A.-E.; data curation, H.A.; writing—original draft preparation, O.H.A.-E., N.S.Z. and H.A.; writing—review and editing, O.H.A.-E. and Q.Z.; visualization, O.H.A.-E., N.S.Z. and H.A.; supervision, O.H.A.-E. and Q.Z.; project administration, O.H.A.-E. and H.A.; funding acquisition, O.H.A.-E. and Q.Z. All authors have read and agreed to the published version of the manuscript.

Funding: This work was supported by the National Natural Science Foundation of China (No. 12274361), the Ministry of Science and Technology Foreign Experts Program (No. QN2021014007L, QN2022014009L), and the Natural Science Foundation of Jiangsu Province (BK20211361, 20KJA430004). This work was also supported by Researchers Supporting Project number RSP2022R468, King Saud University, Riyadh, Saudi Arabia.

Data Availability Statement: The data presented in this study are available on request from the corresponding authors.

Acknowledgments: Authors Thanks Researchers Supporting Project number RSP2022R468, King Saud University, Riyadh, Saudi Arabia.

Conflicts of Interest: There is no conflict of interest to declare.

References

1. Jin, C.; Lin, F.; Suenaga, K.; Iijima, S. Fabrication of a Freestanding Boron Nitride Single Layer and Its Defect Assignments. *Phys. Rev. Lett.* **2009**, *102*, 195505. [[CrossRef](#)] [[PubMed](#)]
2. Meyer, J.C.; Chuvilin, A.; Algara-Siller, G.; Biskupek, J.; Kaiser, U. Selective Sputtering and Atomic Resolution Imaging of Atomically Thin Boron Nitride Membranes. *Nano Lett.* **2009**, *9*, 2683–2689. [[CrossRef](#)] [[PubMed](#)]

3. Song, L.; Ci, L.; Lu, H.; Sorokin, P.B.; Jin, C.; Ni, J.; Kvashnin, A.G.; Kvashnin, D.G.; Lou, J.; Yakobson, B.I.; et al. Large Scale Growth and Characterization of Atomic Hexagonal Boron Nitride Layers. *Nano Lett.* **2010**, *10*, 3209–3215. [[CrossRef](#)] [[PubMed](#)]
4. Kim, K.K.; Hsu, A.; Jia, X.; Kim, S.M.; Shi, Y.; Hofmann, M.; Nezich, D.; Rodriguez-Nieva, J.F.; Dresselhaus, M.; Palacios, T.; et al. Synthesis and Characterization of Hexagonal Boron Nitride Film as a Dielectric Layer for Graphene Devices. *Nano Lett.* **2012**, *6*, 8583–8590. [[CrossRef](#)]
5. Pakdel, A.; Bando, Y.; Golberg, D. Nano boron nitride flatland. *Chem. Soc. Rev.* **2013**, *43*, 934–959. [[CrossRef](#)]
6. Zhou, H.; Zhu, J.; Liu, Z.; Yan, Z.; Fan, X.; Lin, J.; Wang, G.; Yan, Q.; Yu, T.; Ajayan, P.M.; et al. High thermal conductivity of suspended few-layer hexagonal boron nitride sheets. *Nano Res.* **2014**, *7*, 1232–1240. [[CrossRef](#)]
7. Kostoglou, N.; Polychronopoulou, K.; Rebholz, C. Thermal and chemical stability of hexagonal boron nitride (h-BN) nanoplatelets. *Vacuum* **2015**, *112*, 42–45. [[CrossRef](#)]
8. Gao, X.; Wang, S.; Lin, S. Defective Hexagonal Boron Nitride Nanosheet on Ni(111) and Cu(111): Stability, Electronic Structures, and Potential Applications. *ACS Appl. Mater. Interfaces* **2016**, *8*, 24238–24247. [[CrossRef](#)]
9. Watanabe, K.; Taniguchi, T.; Kanda, H. Direct-bandgap properties and evidence for ultraviolet lasing of hexagonal boron nitride single crystal. *Nat. Mater.* **2004**, *3*, 404–409. [[CrossRef](#)]
10. Kubota, Y.; Watanabe, K.; Tsuda, O.; Taniguchi, T. Deep ultraviolet light-emitting hexagonal boron nitride synthesized at atmospheric pressure. *Science* **2007**, *317*, 932–934. [[CrossRef](#)]
11. Haubner, R.; Wilhelm, M.; Weissenbacher, R.; Lux, B. Boron Nitrides—Properties, Synthesis and Applications. In *High Performance Non-Oxide Ceramics II*; Springer: Berlin/Heidelberg, Germany, 2002; pp. 1–45.
12. Eichler, J.; Lesniak, C. Boron nitride (BN) and BN composites for high-temperature applications. *J. Eur. Ceram. Soc.* **2008**, *28*, 1105–1109. [[CrossRef](#)]
13. Dean, C.R.; Young, A.F.; Meric, I.; Lee, C.; Wang, L.; Sorgenfrei, S.; Watanabe, K.; Taniguchi, T.; Kim, P.; Shepard, K.L.; et al. Boron nitride substrates for high-quality graphene electronics. *Nat. Nanotechnol.* **2010**, *5*, 722–726. [[CrossRef](#)] [[PubMed](#)]
14. Geim, A.K.; Grigorieva, I.V. Van der Waals heterostructures. *Nature* **2013**, *499*, 419–425. [[CrossRef](#)] [[PubMed](#)]
15. Wang, J.I.-J.; Yamoah, M.A.; Li, Q.; Karamlou, A.H.; Dinh, T.; Kannan, B.; Braumüller, J.; Kim, D.; Melville, A.J.; Muschinske, S.E.; et al. Hexagonal boron nitride as a low-loss dielectric for superconducting quantum circuits and qubits. *Nat. Mater.* **2022**, *21*, 398–403. [[CrossRef](#)] [[PubMed](#)]
16. Tran, T.T.; Bray, K.; Ford, M.; Toth, M.; Aharonovich, I. Quantum emission from hexagonal boron nitride monolayers. *Nat. Nanotechnol.* **2015**, *11*, 37–41. [[CrossRef](#)]
17. Kim, S.; Fröch, J.E.; Christian, J.; Straw, M.; Bishop, J.; Totonjian, D.; Watanabe, K.; Taniguchi, T.; Toth, M.; Aharonovich, I. Photonic crystal cavities from hexagonal boron nitride. *Nat. Commun.* **2018**, *9*, 2623. [[CrossRef](#)]
18. Fröch, J.E.; Kim, S.; Mendelson, N.; Kianinia, M.; Toth, M.; Aharonovich, I. Coupling Hexagonal Boron Nitride Quantum Emitters to Photonic Crystal Cavities. *ACS Nano* **2020**, *14*, 7085–7091. [[CrossRef](#)]
19. White, S.; Stewart, C.; Solntsev, A.S.; Li, C.; Toth, M.; Kianinia, M.; Aharonovich, I. Phonon dephasing and spectral diffusion of quantum emitters in hexagonal boron nitride. *Optica* **2021**, *8*, 1153. [[CrossRef](#)]
20. Caldwell, D.J.; Kretinin, V.A.; Chen, Y.; Giannini, V.; Fogler, M.M.; Francescato, Y.; Ellis, T.C.; Tischler, G.J.; Woods, R.C.; Giles, J.A.; et al. Sub-diffractive volume-confined polaritons in the natural hyperbolic material hexagonal boron nitride. *Nat. Commun.* **2014**, *5*, 5221. [[CrossRef](#)]
21. Giles, A.J.; Dai, S.; Vurgaftman, I.; Hoffman, T.; Liu, S.; Lindsay, L.; Ellis, C.T.; Assefa, N.; Chatzakis, I.; Reinecke, T.L.; et al. Ultralow-loss polaritons in isotopically pure boron nitride. *Nat. Mater.* **2018**, *17*, 134–139. [[CrossRef](#)]
22. Li, J.; Zhou, G.; Chen, Y.; Gu, B.-L.; Duan, W. Magnetism of C Adatoms on BN Nanostructures: Implications for Functional Nanodevices. *J. Am. Chem. Soc.* **2009**, *131*, 1796–1801. [[CrossRef](#)] [[PubMed](#)]
23. Zeng, H.; Zhi, C.; Zhang, Z.; Wei, X.; Wang, X.; Guo, W.; Bando, Y.; Golberg, D. “White Graphenes”: Boron Nitride Nanoribbons via Boron Nitride Nanotube Unwrapping. *Nano Lett.* **2010**, *10*, 5049–5055. [[CrossRef](#)] [[PubMed](#)]
24. Abdelsalam, H.; Atta, M.M.; Osman, W.; Zhang, Q. Two-dimensional quantum dots for highly efficient heterojunction solar cells. *J. Colloid Interface Sci.* **2021**, *603*, 48–57. [[CrossRef](#)] [[PubMed](#)]
25. Alem, N.; Ramasse, Q.M.; Seabourne, C.R.; Yazyev, O.V.; Erickson, K.; Sarahan, M.C.; Kisielowski, C.; Scott, A.J.; Louie, S.G.; Zettl, A. Subangstrom Edge Relaxations Probed by Electron Microscopy in Hexagonal Boron Nitride. *Phys. Rev. Lett.* **2012**, *109*, 205502. [[CrossRef](#)]
26. Chernozatonskii, L.A.; Demin, V.; Bellucci, S. Bilayered graphene/h-BN with folded holes as new nanoelectronic materials: Modeling of structures and electronic properties. *Sci. Rep.* **2016**, *6*, 38029. [[CrossRef](#)]
27. Payod, R.B.; Saroka, V.A. Ab Initio Study of Absorption Resonance Correlations between Nanotubes and Nanoribbons of Graphene and Hexagonal Boron Nitride. *Semiconductors* **2019**, *53*, 1929–1934. [[CrossRef](#)]
28. Barone, V.; Peralta, J.E. Magnetic Boron Nitride Nanoribbons with Tunable Electronic Properties. *Nano Lett.* **2008**, *8*, 2210–2214. [[CrossRef](#)]
29. Li, L.L.; Yu, X.F.; Yang, X.J.; Zhang, X.H.; Xu, X.W.; Jin, P.; Zhao, J.L.; Wang, X.X.; Tang, C.C. Electronic properties and relative stabilities of heterogeneous edge-decorated zigzag boron nitride nanoribbons. *J. Alloys Compd.* **2015**, *649*, 1130–1135. [[CrossRef](#)]
30. Chopra, N.G.; Luyken, R.J.; Cherrey, K.; Crespi, V.H.; Cohen, M.L.; Louie, S.G.; Zettl, A. Boron Nitride Nanotubes. *Science* **1995**, *269*, 966–967. [[CrossRef](#)]
31. Golberg, D.; Bando, Y.; Tang, C.C.; Zhi, C.Y. Boron Nitride Nanotubes. *Adv. Mater.* **2007**, *19*, 2413–2432. [[CrossRef](#)]

32. Lei, Z.; Xu, S.; Wan, J.; Wu, P. Facile preparation and multifunctional applications of boron nitride quantum dots. *Nanoscale* **2015**, *7*, 18902–18907. [[CrossRef](#)]
33. Kumar, R.; Singh, R.K.; Yadav, S.K.; Savu, R.; Moshkalev, S.A. Mechanical pressure induced chemical cutting of boron nitride sheets into boron nitride quantum dots and optical properties. *J. Alloys Compd.* **2016**, *683*, 38–45. [[CrossRef](#)]
34. Thangasamy, P.; Santhanam, M.; Sathish, M. Supercritical Fluid Facilitated Disintegration of Hexagonal Boron Nitride Nanosheets to Quantum Dots and Its Application in Cells Imaging. *ACS Appl. Mater. Interfaces* **2016**, *8*, 18647–18651. [[CrossRef](#)]
35. Huo, B.; Liu, B.; Chen, T.; Cui, L.; Xu, G.; Liu, M.; Liu, J. One-Step Synthesis of Fluorescent Boron Nitride Quantum Dots via a Hydrothermal Strategy Using Melamine as Nitrogen Source for the Detection of Ferric Ions. *Langmuir* **2017**, *33*, 10673–10678. [[CrossRef](#)] [[PubMed](#)]
36. Peng, D.; Zhang, L.; Li, F.-F.; Cui, W.-R.; Liang, R.-P.; Qiu, J.-D. Facile and Green Approach to the Synthesis of Boron Nitride Quantum Dots for 2,4,6-Trinitrophenol Sensing. *ACS Appl. Mater. Interfaces* **2018**, *10*, 7315–7323. [[CrossRef](#)] [[PubMed](#)]
37. Liu, Q.; Hu, C.; Wang, X. One-pot solvothermal synthesis of water-soluble boron nitride nanosheets and fluorescent boron nitride quantum dots. *Mater. Lett.* **2018**, *234*, 306–310. [[CrossRef](#)]
38. Radhakrishnan, S.; Park, J.H.; Neupane, R.; Reyes, C.A.D.L.; Sudeep, P.M.; Paulose, M.; Martí, A.A.; Tiwary, C.S.; Khabashesku, V.N.; Varghese, O.K.; et al. Fluorinated Boron Nitride Quantum Dots: A New 0D Material for Energy Conversion and Detection of Cellular Metabolism. *Part. Part. Syst. Charact.* **2019**, *36*, 1800346. [[CrossRef](#)]
39. Ahmad, P.; Khandaker, M.U.; Jamil, S.; Rehman, F.; Muhammad, N.; Ullah, Z.; Khan, M.A.R.; Khan, G.; Alotaibi, M.A.; Alharthi, A.I.; et al. Dual role of Magnesium as a catalyst and precursor with enriched boron in the synthesis of Magnesium diboride nanoparticles. *Ceram. Int.* **2020**, *46*, 26809–26812. [[CrossRef](#)]
40. Lin, L.; Xu, Y.; Zhang, S.; Ross, I.M.; Ong, A.C.M.; Allwood, D.A. Fabrication and Luminescence of Monolayered Boron Nitride Quantum Dots. *Small* **2013**, *10*, 60–65. [[CrossRef](#)]
41. Liu, B.; Yan, S.; Song, Z.; Liu, M.; Ji, X.; Yang, W.; Liu, J. One-Step Synthesis of Boron Nitride Quantum Dots: Simple Chemistry Meets Delicate Nanotechnology. *Chem.—A Eur. J.* **2016**, *22*, 18899–18907. [[CrossRef](#)] [[PubMed](#)]
42. Li, Q.; Zheng, Y.; Hou, X.; Yang, T.; Liang, T.; Zheng, J. A wide range photoluminescence intensity-based temperature sensor developed with BN quantum dots and the photoluminescence mechanism. *Sens. Actuators B Chem.* **2020**, *304*, 127353. [[CrossRef](#)]
43. Zhang, X.; An, L.; Bai, C.; Chen, L.; Yu, Y. Hexagonal boron nitride quantum dots: Properties, preparation and applications. *Mater. Today Chem.* **2021**, *20*, 100425. [[CrossRef](#)]
44. Abdelsalam, H.; Elhaes, H.; Ibrahim, M. Tuning electronic properties in graphene quantum dots by chemical functionalization: Density functional theory calculations. *Chem. Phys. Lett.* **2018**, *695*, 138–148. [[CrossRef](#)]
45. Abdelsalam, H.; Saroka, V.A.; Ali, M.; Teleb, N.H.; Elhaes, H.; Ibrahim, M.A. Stability and electronic properties of edge functionalized silicene quantum dots: A first principles study. *Phys. E Low-Dimens. Syst. Nanostructures* **2018**, *108*, 339–346. [[CrossRef](#)]
46. Nguyen, V.; Yan, L.; Zhao, N.; van Canh, N.; Hang, N.T.N.; Le, P.H. Tuning photoluminescence of boron nitride quantum dots via surface functionalization by femtosecond laser ablation. *J. Mol. Struct.* **2021**, *1244*, 130922. [[CrossRef](#)]
47. Krepel, D.; Kalikhman-Razvozov, L.; Hod, O. Edge Chemistry Effects on the Structural, Electronic, and Electric Response Properties of Boron Nitride Quantum Dots. *J. Phys. Chem. C* **2014**, *118*, 21110–21118. [[CrossRef](#)]
48. Liu, Y.; Bhowmick, S.; Yakobson, B.I. BN White Graphene with “Colorful” Edges: The Energies and Morphology. *Nano Lett.* **2011**, *11*, 3113–3116. [[CrossRef](#)]
49. Zhang, J.; Zhao, W.; Zhu, J. Missing links towards understanding the equilibrium shapes of hexagonal boron nitride: Algorithm, hydrogen passivation, and temperature effects. *Nanoscale* **2018**, *10*, 17683–17690. [[CrossRef](#)]
50. Xi, Y.; Zhao, M.; Wang, X.; Li, S.; He, X.; Wang, Z.; Bu, H. Honeycomb-Patterned Quantum Dots beyond Graphene. *J. Phys. Chem. C* **2011**, *115*, 17743–17749. [[CrossRef](#)]
51. Xu, P.; Yu, S.S.; Qiao, L. Electronic properties of a patchwork of armchair graphene nanoribbon and triangular boron nitride nanoflake. *Mol. Simul.* **2013**, *39*, 487–494. [[CrossRef](#)]
52. Xi, Y.; Zhao, X.; Wang, A.; Wang, X.; Bu, H.; Zhao, M. Tuning the electronic and magnetic properties of triangular boron nitride quantum dots via carbon doping. *Phys. E Low-Dimens. Syst. Nanostructures* **2013**, *49*, 52–60. [[CrossRef](#)]
53. Yamijala, S.S.; Bandyopadhyay, A.; Pati, S.K. Structural Stability, Electronic, Magnetic, and Optical Properties of Rectangular Graphene and Boron Nitride Quantum Dots: Effects of Size, Substitution, and Electric Field. *J. Phys. Chem. C* **2013**, *117*, 23295–23304. [[CrossRef](#)]
54. Yamijala, S.S.; Bandyopadhyay, A.; Pati, S.K. Electronic properties of zigzag, armchair and their hybrid quantum dots of graphene and boron-nitride with and without substitution: A DFT study. *Chem. Phys. Lett.* **2014**, *603*, 28–32. [[CrossRef](#)]
55. Chakraborty, D.; Chattaraj, P.K. Effect of functionalization of boron nitride flakes by main group metal clusters on their optoelectronic properties. *J. Physics Condens. Matter* **2017**, *29*, 425201. [[CrossRef](#)] [[PubMed](#)]
56. Degheidy, A.R.; Elkenany, E.B. Pressure and composition dependence of electronic, optical and mechanical properties of GaP Sb1– alloys. *Thin Solid Films* **2016**, *599*, 113–118. [[CrossRef](#)]
57. Pan, C.; Long, M.; He, J. Enhanced thermoelectric properties in boron nitride quantum-dot. *Results Phys.* **2017**, *7*, 1487–1491. [[CrossRef](#)]
58. Xie, B.; Liu, H.; Hu, R.; Wang, C.; Hao, J.; Wang, K.; Luo, X. Targeting Cooling for Quantum Dots in White QDs-LEDs by Hexagonal Boron Nitride Platelets with Electrostatic Bonding. *Adv. Funct. Mater.* **2018**, *28*, 1801407. [[CrossRef](#)]

59. Zhou, S.; Ma, Y.; Zhang, X.; Lan, W.; Yu, X.; Xie, B.; Wang, K.; Luo, X. White-Light-Emitting Diodes from Directional Heat-Conducting Hexagonal Boron Nitride Quantum Dots. *ACS Appl. Nano Mater.* **2019**, *3*, 814–819. [[CrossRef](#)]
60. Bandyopadhyay, A.; Yamijala, S.S.R.K.C.; Pati, S.K. Tuning the electronic and optical properties of graphene and boron-nitride quantum dots by molecular charge-transfer interactions: A theoretical study. *Phys. Chem. Chem. Phys.* **2013**, *15*, 13881–13887. [[CrossRef](#)]
61. Chakraborty, D.; Chattaraj, P.K. Sequestration and Activation of Small Gas Molecules on BN-Flakes and the Effect of Various Metal Oxide Molecules therein. *J. Phys. Chem. C* **2016**, *120*, 27782–27799. [[CrossRef](#)]
62. Neek-Amal, M.; Beheshtian, J.; Sadeghi, A.; Michel, K.H.; Peeters, F.M. Boron Nitride Monolayer: A Strain-Tunable Nanosensor. *J. Phys. Chem. C* **2013**, *117*, 13261–13267. [[CrossRef](#)]
63. Matsoso, J.B.; Garcia-Martinez, C.; Mongwe, H.T.; Tourey, B.; Serbena, M.P.J.; Journet, C. Room temperature ammonia vapour detection on hBN flakes. *J. Phys. Mater.* **2021**, *4*, 044007. [[CrossRef](#)]
64. Abdelsalam, H.; Younis, W.O.; Saroka, V.A.; Teleb, N.H.; Yunoki, S.; Zhang, Q. Interaction of hydrated metals with chemically modified hexagonal boron nitride quantum dots: Wastewater treatment and water splitting. *Phys. Chem. Chem. Phys.* **2020**, *22*, 2566–2579. [[CrossRef](#)] [[PubMed](#)]
65. Xue, Y.; Dai, P.; Jiang, X.; Wang, X.; Zhang, C.; Tang, D.; Weng, Q.; Wang, X.; Pakdel, A.; Tang, C.; et al. Template-free synthesis of boron nitride foam-like porous monoliths and their high-end applications in water purification. *J. Mater. Chem. A* **2016**, *4*, 1469–1478. [[CrossRef](#)]
66. Ikram, M.; Hassan, J.; Imran, M.; Haider, J.; Ul-Hamid, A.; Shahzadi, I.; Ikram, M.; Raza, A.; Kumar, U.; Ali, S. 2D chemically exfoliated hexagonal boron nitride (hBN) nanosheets doped with Ni: Synthesis, properties and catalytic application for the treatment of industrial wastewater. *Appl. Nanosci.* **2020**, *10*, 3525–3528. [[CrossRef](#)]
67. Osman, W.; Abdelsalam, H.; Ali, M.; Teleb, N.; Yahia, I.; Ibrahim, M.; Zhang, Q. Electronic and magnetic properties of graphene quantum dots doped with alkali metals. *J. Mater. Res. Technol.* **2021**, *11*, 1517–1533. [[CrossRef](#)]
68. Abdelsalam, H.; Zhang, Q.F. Properties and applications of quantum dots derived from two-dimensional materials. *Adv. Phys. X* **2022**, *7*, 2048966. [[CrossRef](#)]
69. Park, H.; Wadehra, A.; Wilkins, J.W.; Neto, A.H.C. Magnetic states and optical properties of single-layer carbon-doped hexagonal boron nitride. *Appl. Phys. Lett.* **2012**, *100*, 253115. [[CrossRef](#)]
70. Tan, B.; Wu, Y.; Gao, F.; Yang, H.; Hu, Y.; Shang, H.; Zhang, X.; Zhang, J.; Li, Z.; Fu, Y.; et al. Engineering the Optoelectronic Properties of 2D Hexagonal Boron Nitride Monolayer Films by Sulfur Substitutional Doping. *ACS Appl. Mater. Interfaces* **2022**, *14*, 16453–16461. [[CrossRef](#)]
71. Hayee, F.; Yu, L.; Zhang, J.L.; Ciccarino, C.J.; Nguyen, M.; Marshall, A.F.; Aharonovich, I.; Vučković, J.; Narang, P.; Heinz, T.F.; et al. Revealing multiple classes of stable quantum emitters in hexagonal boron nitride with correlated optical and electron microscopy. *Nat. Mater.* **2020**, *19*, 534–539. [[CrossRef](#)]
72. Mendelson, N.; Chugh, D.; Reimers, J.R.; Cheng, T.S.; Gottscholl, A.; Long, H.; Mellor, C.J.; Zettl, A.; Dyakonov, V.; Beton, P.H.; et al. Identifying carbon as the source of visible single-photon emission from hexagonal boron nitride. *Nat. Mater.* **2021**, *20*, 321–328. [[CrossRef](#)] [[PubMed](#)]
73. Frisch, M.E.; Trucks, G.W.; Schlegel, H.B.; Scuseria, G.E.; Robb, M.A.; Cheeseman, J.R.; Scalmani, G.; Barone, V.P.G.A.; Petersson, G.A.; Nakatsuji, H.J.R.A.; et al. *Gaussian 16, Revision B.01*; Gaussian, Inc.: Wallingford, CT, USA, 2016.
74. Becke, A.D. Density-functional thermochemistry. III. The role of exact exchange. *J. Chem. Phys.* **1993**, *98*, 5648–5652. [[CrossRef](#)]
75. Lee, C.; Yang, W.; Parr, R.G. Development of the Colle-Salvetti correlation-energy formula into a functional of the electron density. *Phys. Rev. B* **1998**, *37*, 785–789. [[CrossRef](#)] [[PubMed](#)]
76. Ditchfield, R.; Hehre, W.J.; Pople, J.A. Self-Consistent Molecular-Orbital Methods. IX. An Extended Gaussian-Type Basis for Molecular-Orbital Studies of Organic Molecules. *J. Chem. Phys.* **1971**, *54*, 724–728. [[CrossRef](#)]
77. Rassolov, V.A.; Ratner, M.A.; Pople, J.A.; Redfern, P.C.; Curtiss, L.A. 6-31G* basis set for third-row atoms. *J. Comput. Chem.* **2001**, *22*, 976–984. [[CrossRef](#)]
78. Grimme, S.; Antony, J.; Ehrlich, S.; Krieg, H. A consistent and accurate ab initio parametrization of density functional dispersion correction (DFT-D) for the 94 elements H-Pu. *J. Chem. Phys.* **2010**, *132*, 154104–154119. [[CrossRef](#)]
79. Abdelsalam, H.; Osman, W.; Elkader, O.H.A.; Zhang, Q. Vibrationally-resolved absorption and fluorescence spectra of chemically modified 2D hexagonal boron nitride quantum dots. *Chem. Phys. Lett.* **2022**, *806*, 140025. [[CrossRef](#)]
80. Leenaerts, O.; Partoens, B.; Peeters, F.M. Adsorption of H₂O, NH₃, CO, NO₂, and NO on graphene: A first-principles study. *Phys. Rev. B* **2008**, *77*, 125416. [[CrossRef](#)]
81. Szarek, P.; Suwannawong, S.; Doi, K.; Kawano, S. Theoretical Study on Physicochemical Aspects of a Single Molecular Junction: Application to the Bases of ssDNA. *J. Phys. Chem. C* **2013**, *117*, 10809–10817. [[CrossRef](#)]
82. El-Mansy, M.A.M.; Osman, W.; Abdelsalam, H. The electronic and optical absorption properties of pristine, homo and hetero Bi-nanoclusters. *Chem. Phys.* **2021**, *544*, 111113. [[CrossRef](#)]
83. Donarelli, M.; Ottaviano, L. 2D Materials for Gas Sensing Applications: A Review on Graphene Oxide, MoS₂, WS₂ and Phosphorene. *Sensors* **2018**, *18*, 3638. [[CrossRef](#)] [[PubMed](#)]